Design of an AI-Enhanced Medical Research-Informed Multi-Sensor-Based Online Physical Education Motion Capture System

Zhilong Zhao[1] and Xinyang Xing[2*]

[1]Dean's Office, Hebei Sport University, Shijiazhuang, 050041, Hebei Province, China
[1]zhaozhilong@hepec.edu.cn
[2]Physical Education Department, Hebei Sport University, Shijiazhuang, 050041, Hebei province, China, [2]2013004@hepec.edu.cn

Corresponding author: Xinyang Xing, 2013004@hepec.edu.cn

Abstract. Online physical education has increasingly gained public attention due to China's growing interest in this kind of instruction. However, the growth of online physical education has its challenges. For instance, due to the limits of the objective site, teaching outcomes for online physical education courses are not satisfactory because students cannot watch all course components. Without expanding the current teaching volume, a new teaching strategy built on a multi-sensor motion capture system is suggested to overcome these issues. The outcomes of the experiments demonstrate that the proposed motion capture technology can significantly boost motion capture's effectiveness in online physical education.

1 INTRODUCTION

The goal of traditional physical education, backed by physical education theories, is for students to become proficient in sports techniques. To achieve this goal, students must become proficient in biological education knowledge and sports skills through traditional classroom sports[23]. This method of instruction is frequently teacher-centered, pursuing students' precise mastery of sports technology with vital timeliness, often ignoring the individual differences resulting from students' various physical characteristics and missing the exploration of students' potential in sports, which is not conducive to the overall improvement of students' sports quality[14].

Using online physical education, which shifts the focus of the classroom from the teacher to the students, is a creative way to pique kids' interest and enthusiasm for sports. The primary method of online physical education is for the teacher to transmit sports knowledge, biological education

knowledge, and after-school materials to the students via the Internet. The students then take the initiative to learn and accept the knowledge and skills related to physical education, and the teacher can respond to their questions promptly[10].

Physical education involves many challenging technical motions, and these movements' temporary and unique aspects make teaching them more difficult. The biologically accurate standard strength of movements can be precisely measured by the multi-sensor-based movement capture system, which theoretically realizes the ideal balance of strength and control. Individual differences can then be combined to create customized training programs, attack strategies, body protection manuals, etc.[20].

The introduction of a multi-sensor motion capture system can, in the first place, digitize the learning process of movements that must be repeatedly simulated, enabling students to move from simulating movements' superficial appearances to understanding their essence; in the second place, it can delay the presentation of realistic transient and complex movements in all aspects, effectively resolving the learning challenges brought on by the observation angle [11]. As a last option, it can convert further "unexplainable" teaching linkages into a fully digital teaching process. Let the teachers' instruction be quantitative, the students' learning be targeted, the teaching evaluation be based on the available data, and then create a new, open, transparent, and digital system for learning and teaching[13].

As a result, this study begins by outlining the theory behind the multi-sensor-based posture solution. It is initially essential to realize single-node pose solving to learn a multi-sensor-based multi-node online physical education motion capture system. Several academics have suggested pertinent algorithms for this step[8]. Our analysis and comparison in this study reveals that, despite these algorithms using essentially the same concept, they employ various mathematical calculation techniques, ultimately resulting in varying computational efficiency[22],[17].

2   RELATED WORK

Most online physical education instruction for the current home setting is delivered through online learning platforms. These websites can offer reliable and excellent learning resources for the learning community. The majority of online resources for physical education, 56.2%, are in the form of videos. In comparison, 43.8% are documents, slides, and PDF files with lesson plans, sample exercises, and reference materials as their primary features[6]. Additionally, 96% of the physical education videos were updated after 2013, demonstrating the emphasis online physical education places on video resources. As a result, video teaching will overtake other delivery methods for online physical education in China.

As early as 1997, the United States started investigating the first physical education online. As distance learning quickly took off in the twenty-first century, up to 700,000 students in the United States' K–12 schools registered for online classes in 2004–2005, and by 2009, that number had surpassed 1 million[12]. Ongoing research and practice have improved the issue of uneven physical education resources, and specific accomplishments have been made.

China started studying sensor technology in-depth in the early 1990s, and after fifty years of work, it has steadily learned nearly all of the pertinent subjects in the field [16]. Traditional multi-sensors are primarily employed in navigation, aerospace, and military vehicles that navigate on land. Despite their excellent accuracy, these devices' substantial mass, enormous size, and requirement for extensive initial calibration before usage severely restrict their use and popularity [16]. Due to their lower cost, smaller size and power consumption, higher precision, and better integration, multi-sensors have progressively begun to be marketed as the best option for data acquisition modules in motion capture systems with the rapid development of MEMS technology.

Numerous research organizations have studied the wireless multi-sensor-based human motion capture system that China developed [7],[4]. The overseas Draper Lab, Litton Lab, MIT, etc, have also done in-depth studies on motion capture systems. The Moven inertial motion capture system from Xsens in the Netherlands, the 3Dsuit inertial motion capture system from Innlabs, and the Perception Neuron motion capture system from Noitom in China are examples of representative commercial products[1]. The Innlabs 3Dsuit inertial motion capture system uses OSv3 multi-sensor to provide a full-body set, tethered set, and a built-in set of three sets of nodes, respectively, 10-sensor set, 7-sensor set, and 5-sensor set of motion capture solution system, depending on the diverse requirements of users[24]. Support for real-time viewing, recording, and replaying motion capture data and synchronous motion capture for two and multiple players. The first inertial motion capture system to leverage the MTX multi-sensor and wireless Xbus system is Xsens' MVN Animate. The standard motion capture system has data drift issues when both feet are off the ground at once, jumping, etc. Still, this system is the only one on the market immune to magnetic field interference. The physical diagram of the Xsens MVN motion capture system is shown in Figure 1.

Figure 1: Xsens MVN motion capture system.

The SharkStream motion capture system, displayed at the World Consumer Electronics Show (CES) in Las Vegas, has a battery life of one day and broadcasts wirelessly through two antennas over more than 250 meters[2]. They separately created a communication protocol that is incorporated into the system and has improved algorithmic correctness. The most portable, adaptable, and affordable high-performance motion capture device available is Noitom's Perception Neuron, as seen in Figure 2. Perception Neuron's great precision and low latency make the reproduction of trajectories more natural and smooth, and it is also the most user-friendly motion capture system in the world to date [25].

Figure 2: Noitom perception neuron motion capture system.

3   SYSTEM DESIGN

The design objective of this paper is to create a motion capture system for online physical education based on multiple sensors that must be able to track human whole body motions for any movements of the natural human body to be reflected on the host computer's 3D character model. The data gathering, communication, processing, and restoration components of the measurement-based whole-body online physical education motion capture system are the primary ones. Data processing is the fusion of the data from three sensors, or pose solving; the data restoration principle represents the entire body movement on the virtual 3D character model, including skeletal animation and joint calibration of multiple sensor nodes. Data acquisition consists of node sensors and Hub aggregation nodes deployed in various human body parts.

The design of this paper must adhere to the following criteria, in addition to the previous study of the requirements of the motion capture system for online physical education.

1. Hardware part: ten inertial sensing nodes composed of multiple sensors, a Hub aggregation transmission node, and a data receiving module.

2. Software: skeleton animation drawing algorithm, joint calibration algorithm of multi-node sensors, posture solving algorithm based on data fusion from three sensors, accelerometer, gyroscope, and magnetometer-based sensor calibration technique.

In conclusion, the main objective of this study is to develop an inertial online physical education motion capture system that can simultaneously record the entire body's motion using a combination of motion capture-related algorithms and structures. Figure 3 depicts the system architecture used in this paper.
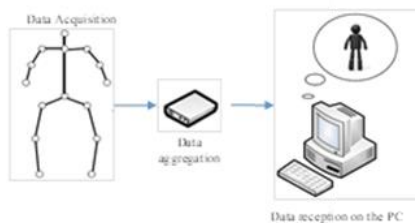
Figure 3: Full-body online physical education motion capture system architecture.

Because of its nature and underlying design philosophy, the sensor is a mechanical construction vulnerable to interference. Additionally, it is impossible to glue the PCB components to keep the sensor level with the PCB board, which results in unavoidable mistakes that may cause the sensor to drift to zero. To calibrate the accelerometer, gyroscope, and magnetometer, this section will employ the gravity reference calibration method, the field calibration method of determining the mean value to correct the drift zero point, and the ellipse fitting method.

3.1   Accelerometer Calibration

According to the number of input axes, accelerometer sensors can be capacitive, thermal inductive, or piezoelectric and are categorized as single-axis, dual-axis, and tri-axis accelerometers. Accelerometers are frequently employed in aerospace, robotics, and automotive applications because of their tiny size and lightweight, which enables them to measure spatial acceleration and accurately represent the motion of an object. As inertial sensing equipment, low-cost triaxial accelerometers are frequently utilized in attitude tracking. However, the accelerometers may reduce the system's measuring precision because of the unavoidable faults brought by human welding

installation. Therefore, The accelerometers are compensated for measurement inaccuracies brought on by issues like non-perpendicularity of the triaxial accelerometers' coordinate axes to acquire more accurate acceleration data.

   1. Gravity reference calibration method

The gravity reference calibration method, the second non-instrumentation calibration technique, was selected for this paper. When installed statically, the local gravitational acceleration should always be the accelerometer's measured value. At this point, the three-axis measurement of the accelerometer should be the local acceleration of gravity in the three axes of the component, which can be determined using the vector approach as given in equation (1).

$$acc_x^2 + acc_y^2 + acc_z^2 = G^2 \tag{1}$$

However, issues like the accelerometer coordinate axes' non-perpendicularity result in a shift in the triaxial data. This is how the accelerometer's mathematical error model is created.

$$\begin{bmatrix} D_x \\ D_y \\ D_z \end{bmatrix} = \begin{bmatrix} S_x & k_{xy} & k_{xz} \\ k_{yx} & S_y & k_{yz} \\ k_{zx} & k_{zy} & S_z \end{bmatrix} \begin{bmatrix} M_x \\ M_y \\ M_z \end{bmatrix} + \begin{bmatrix} B_x \\ B_y \\ B_z \end{bmatrix} \tag{2}$$

D is the actual acceleration value; S is the sensor scale factor; k is the installation error factor. In practical applications, the small installation error coefficient about the scale factor and zero deviation is usually ignored, so the accelerometer's error model is simplified, as shown in equation (3).

$$\begin{bmatrix} D_x \\ D_y \\ D_z \end{bmatrix} = \begin{bmatrix} S_x & 0 & 0 \\ 0 & S_y & 0 \\ 0 & 0 & S_z \end{bmatrix} \begin{bmatrix} M_x \\ M_y \\ M_z \end{bmatrix} + \begin{bmatrix} B_x \\ B_y \\ B_z \end{bmatrix} \tag{3}$$

In the calibration process, the accelerometer is first placed at rest, moved slowly, and held in each face for some time. The data of the upper, lower, left, right, front, and rear six faces are measured as the measured acceleration vector M; secondly, the reference vector D is calculated, as shown in equation (4).

$$D = \begin{bmatrix} g & 0 & 0 \\ -g & 0 & 0 \\ 0 & g & 0 \\ 0 & -g & 0 \\ 0 & 0 & g \\ 0 & 0 & -g \end{bmatrix} \tag{4}$$

Then, the maximum and minimum data of gravitational acceleration on each axis are used to find the average value to get the offset of each axis, as shown in equation (5).

$$B = \frac{M[max] + M[min]}{2} \tag{5}$$

Finally, the actual measured acceleration M and equations (4) and (5) are brought into the measurement model equation (3), and the linear equation system is solved; that is, the calibration of the accelerometer is completed. Since the error of the accelerometer is only influenced by the nature of the device itself, the calibration of the accelerometer is usually done only once.

3.2   Gyroscope Calibration

Gyroscope (Gyroscope) measures the angle between the carrier and the vertical axis of its internal gyro rotor to determine the motion's angular velocity. A three-axis gyroscope's angle and angular velocity can choose the carrier's motion in three-dimensional space. Still, the carrier's orientation

relative to the Earth's surface cannot be determined. The three-axis gyroscope is the most critical sensitive component in the measurement of online physical education motion capture systems, and the precision of its measurement directly influences the precision of pose resolution in these systems. Recalibration is needed at each power-up to get the best performance out of the gyroscope because it is highly subject to external factors, particularly temperature.

1. Field calibration method

The mathematical model of the gyroscope is established as shown in equation (6).

$$\begin{bmatrix} G_x \\ G_y \\ G_z \end{bmatrix} = \begin{bmatrix} g_{0x} \\ g_{0y} \\ g_{0z} \end{bmatrix} + \begin{bmatrix} g_x \\ g_y \\ g_z \end{bmatrix} + \begin{bmatrix} v_{gx} \\ v_{gy} \\ v_{gz} \end{bmatrix} \tag{6}$$

Gyroscope calibration focuses primarily on correcting the zero bias compared to the zero bias, ignoring the small amount of random error because the gyroscope will experience zero point drift when the temperature changes. In the calibration process, firstly, the node sensor is left for some time, and the zero output value of the gyroscope is collected several times. Secondly, the obtained data is averaged by equation (5) to get the zero bias value of the gyroscope g_0; finally, according to the mathematical model equation (6), the calibration of the gyroscope can be completed.

$$\omega_c = \frac{1}{k} \left[\sum_{i=1}^{k} \omega_i \right] \tag{7}$$

3.3 Magnetometer Calibration

The Earth naturally has a magnetic field, which is a vector field with a direction pointing from the magnetic south pole to the magnetic north pole. Direct use of the magnetometer can cause significant measurement errors due to the device's limitations and susceptibility to interference from the magnetic field around it, so the magnetometer needs to be corrected for mistakes to obtain more accurate measurement data.

1. Ellipse fitting method

By measuring the angle between the carrier and the magnetic field, the magnetometer determines the carrier's three-dimensional spatial position because the gravitational, magnetic field of the Earth is known. If the environment does not change, the X, Y, and Z axes inside the magnetometer sensor should all be perpendicular. The projected trajectory of the observed values should form a sphere in three dimensions when the sensor-equipped device is spun in all directions. The sphere's radius should correspond to the strength of the local magnetic field. But in reality, problems like zero bias and the three axes' non-orthogonality impact the magnetometer.

Theoretically, given that the center of the sphere is currently offset from the origin, the data collected by the magnetometer in the same plane in the positive and negative directions of the magnetic field should have the same size and opposite sign. Additionally, the model should be a sphere with the origin at its center. Create the magnetometer's mathematical model according to equation (8).

$$M = mag_{offs} + m + v_m \tag{8}$$

Where M is the measured value of the magnetometer, mag_{offs} is the offset of the magnetometer, m is the actual value, and v_m is the random error. Similar to the accelerometer and gyroscope, the offset of the magnetometer is calculated by ignoring a small amount of unexpected error. In the above experiment, the offset of the three axes is found by traversing, as shown in equation (9), after rotating in each direction.

$$mag_{offs} = \frac{mag_{max} + mag_{min}}{2} \tag{9}$$

The offset calculated in equation (9) is then substituted into the mathematical model of the magnetometer, and the data for each axis is subtracted from the corresponding X-axis, Y-axis, and Z-axis offsets to complete the magnetometer calibration. The calibration of the magnetometer is the same as that of the accelerometer. If no sizeable magnetic interference exists, calibration is only needed once.

3.4 Attitude Solution

In this paper, Madgwick's algorithm is used, which is essentially a weighted integration of the attitude $^S_E q_{\omega,t}$ calculated by the gyroscope at time t and the attitude $^S_E q_{\nabla,t}$ calculated by the accelerometer and magnetometer together to obtain the final attitude angle $^S_E q_{est,t}$. The formula gives the weighting factor γ_1 calculated by the gyroscope.

$$\gamma_1 = 1 - \frac{\beta \Delta t}{\beta \Delta t + \mu} \tag{10}$$

The error value β per unit time of the gyroscope is very small, and $\beta \Delta t$ is generally used to express the error of the gyroscope. The weighting factor γ_2 jointly calculated by the accelerometer, and the formula gives the magnetometer.

$$\gamma_2 = 1 - \frac{\mu}{\beta \Delta t + \mu} \tag{11}$$

The attitude angle error calculated by the accelerometer and magnetometer is determined by different calculation methods, usually Newtonian, Gaussian Newtonian iterative, gradient descent, conjugate gradient, etc. The Madgwick algorithm uses the gradient descent method. The error is the step size μ selected in the gradient descent method, and the longer the μ, the larger the error. In summary, the overall error of the system is $\beta \Delta t + \mu$.

1. Step size μ

The step size μ is adjustable; the more petite the μ, the more iterations, and the higher the accuracy of the final result. Multiple iterations are computationally intensive, so in practical engineering, they are usually simplified, and the best estimate is approximated by one iteration when the step size is shown in equation (12).

$$\mu = \eta \left\| ^S_E \dot{q}_{\omega,t-1,t} \right\| \Delta t, \eta > 1 \tag{12}$$

Where the size of η is adjusted according to the actual situation and used to compensate for the measurement errors of the accelerometer and magnetometer, the change in attitude angle from moment minus 1 to moment is shown in equation (13).

$$^S_E \dot{q}_{\omega,t-1,t} = \frac{1}{2} {}^S_E \hat{q}_{est,t-1} \cdot {}^S \omega_t \tag{13}$$

2. Gyroscope $^S_E q_{\omega,t}$

The angular velocity of each of the three axes measured by the gyroscope is represented by $\omega_x, \omega_y, \omega_z$, which can be regarded as a quaternion with zero fundamental part, i.e.

$$s\omega = [0 \quad \omega_x \quad \omega_y \quad \omega_z] \tag{14}$$

The rate of change of the attitude quaternion $^S_E \hat{q}$ is related to the current attitude and angular velocity and is calculated as follows.

$$\frac{S}{E}\hat{q} = \frac{1}{2}\frac{S}{E}q \cdot {}^{S}\omega \tag{15}$$

In practical engineering, the system sampling interval should be the lowest sampling rate among the three sensors due to their different maximum adoption rates. Figure 4 shows the block diagram of the pose solution based on the gradient descent method.
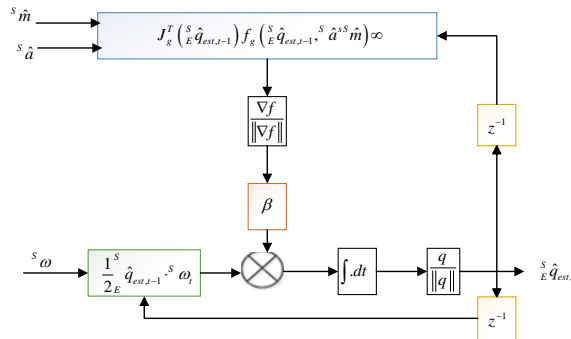
Figure 4: Block diagram of pose solution based on gradient descent method.

4 EXPERIMENTS

4.1 Data Communication Test

Table 1 shows the results of the 60-second continuous communication test. The ten nodes must be split into four transmissions because each report can only transmit data from three nodes and has a length of 58 bytes. The time between each transmission is 5 ms, so 60 seconds will produce 679.7K bytes. This corresponds to the findings of the actual tests and shows that the entire communication link is smooth and capable of meeting the system's communication needs.
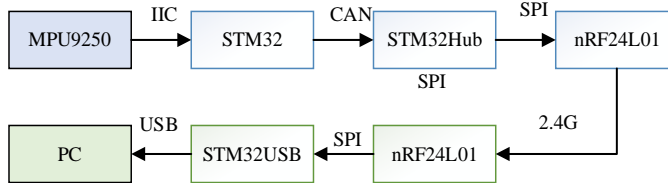
Figure 5: Flow chart of sensor data transfer to PC.

Test item	Theoretical requirements	Experimental results
Correctness	Received 1-180	Received 1-180
Rate	Received 679.7K data	Received 679.7K data

Table 1: Comparison table of communication capability test results.

4.2 System Functionality Testing

The investigation shows that a single node's performance significantly affects the system as a whole. The system's three subsequent components—sensor data analysis, sensor calibration, and single node posture capture—are confirmed and put to the test.

4.2.1 Accelerometer Raw Data Analysis

The USB interface uses a USB 3.0 interface, and a 3.7V lithium battery powers the wear circuit. Node 2 was selected as the node for the test, powered on, and data was recorded to a file. First, the whole node was allowed to stand still, and the static performance of the three sensors was analyzed. The sensors were always stationary during the experiment, and the recorded frequency was 40Hz. Figure 6 shows the output of the X-axis of node #2 in the fixed condition. As can be seen in Figure 6, the accelerometer is very noisy, even in the static case. The sizeable static noise is due to various process aspects and electromagnetic interference.
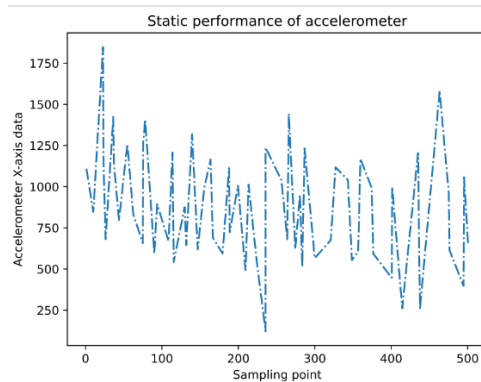
Figure 6: Noise in the static case of the accelerometer.
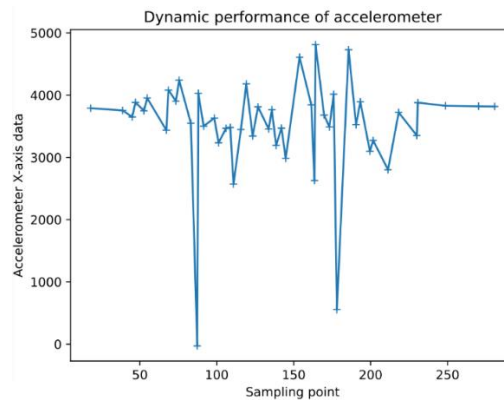
Figure 7: Noise in the dynamic case of the accelerometer.

In addition, the accelerometer is the sensor that measures the accelerometer of the object's motion. If the object is not stationary concerning the Earth itself, the noise of the accelerometer subjected to motion will be even greater. Sensor #2 is placed horizontally, i.e., the Y-axis sensor is positioned vertically upwards, and then the sensor is rotated around the Y-axis for one week, and the acquired data is recorded. Figure 7 shows the data output from the X-axis of the accelerometer. Theoretically, when rotating around the Z-axis at a uniform speed, the data output from the X-axis should be 0. Acceleration is introduced in the X-axis because of the inability to guarantee absolute consistent rotation during the rotation. From Figure 7, we can see that the noise in the dynamic case is very high and may even lead to sensor saturation. Therefore, the accelerometer alone cannot measure

the attitude of the target object. Table 2 shows a comparison table of the peak-to-peak values for the two cases above. Theoretically, the output in the static case of the Z-axis is 32767.

Parameters	Dynamic	Static
Peak to Peak	19305	215

Table 2: Comparison of peak-to-peak values for the dynamic and static cases of the accelerometer.

4.2.2 Analysis of Raw Gyroscope Data

Aerospace and robotics both extensively use gyroscopes. Gyroscope technology has progressed to include mechanical, laser, and MEMS versions. Mechanical gyroscopes, for example, are frequently employed for missile navigation but are too big to be used in applications with severe volume requirements. Although laser gyroscopes are more costly and smaller than mechanical gyroscopes, they cannot be employed in motion capture systems.

This system uses the integrated gyroscope MPU9250. The information gathered by the gyroscope is checked and tested in this subsection. A 3.7V lithium battery powers the wearable circuit, and the USB interface employs a USB 3.0 interface. A node was chosen and kept still to gather information from the three axes. Data collection occurs at 40 Hz and takes around a minute.
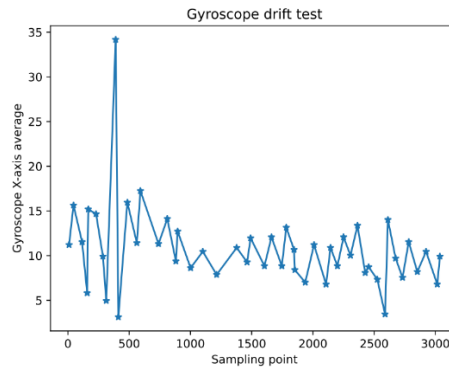
Figure 8: Gyroscope static drift test.

Figure 8 demonstrates that the gyroscope of MEMS has a high noise level and will occasionally show strange spikes. If this data is integrated straight away, the noise that builds up over time will get bigger and bigger. Drift phenomenon, motion, temperature fluctuations, and integration errors impact the gyroscope. The so-called drift is the gradual detachment of the gyroscope's output from zero at rest. The gyroscope data is mean filtered here with a window size of 25, allowing for precise observation of the gyroscope drift phenomenon. Figure 9 shows that the gyroscope has drifted noticeably in the wrong direction after just one minute. Even if there is no integration error, the gyroscope's baseline drift will cause the integration result error to increase.

4.2.3 Angle Tracking Test

Evaluating the single node's angle tracking is necessary before considering the multi-node motion capture system since the single node's performance directly impacts the multi-node system's performance. According to theory, the three Euler angles discovered using single-node tracking should be constant while the target object is stationary.
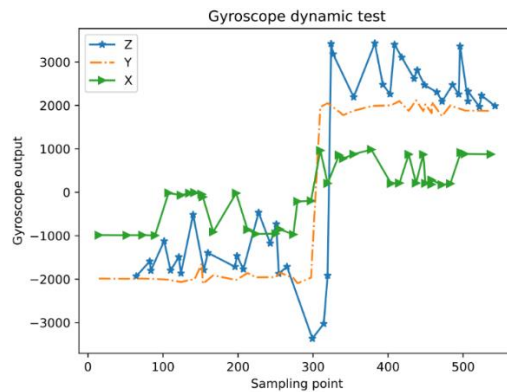
Figure 9: Gyroscope dynamic test.

The heading angle will continue to increase in a specific direction without the geomagnetic meter's correction of the heading angle. Here is a comparison of the MARG mode with and without the geomagnetic meter turned on.

The comparison of the heading, pitch, and cross-roll angles in the two tests is shown in Figures 10 and 11. Figure 10 shows a significant difference between the geomagnetic meter's final result when enabled and when not. While the heading angle inaccuracy of the IMU mode without the geomagnetic meter activated continuously increases, the heading angle with the geomagnetic meter allowed also fluctuates constantly around 0 degrees. Additionally, it can be shown that the inaccuracy in the heading angle of the IMU mode without the geomagnetic meter activated increases linearly with time, further demonstrating that the integration is the primary cause of the heading angle error. Any system that needs a heading angle would not accept an increase in heading angle error without developing the geomagnetic meter.
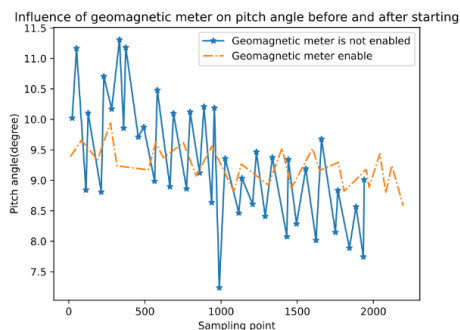
Figure 10: Effect of geomagnetic meter on pitch angle before and after activation.

A graphic of the geomagnetic meter's impact on the two remaining angles before and after it is enabled is shown in Figure 11. The drift in pitch and cross-roll angles before the geomagnetic meter is enabled is minimal compared to the change in heading angle in Figure 11. Additionally, these two angles are noisy and are influenced by the accelerometer. The noise of these two angles and the drift issue were significantly decreased after the geomagnetic meter was turned on. It is evident from the test results above that the geomagnetic meter effectively lowers noise and eradicates heading angle inaccuracy. The root-mean-square errors of the three Euler angles under static

conditions in IMU mode and MARG mode are displayed in Table 3. The table shows that adding the geomagnetic meter alters the precision of the three Euler angles.
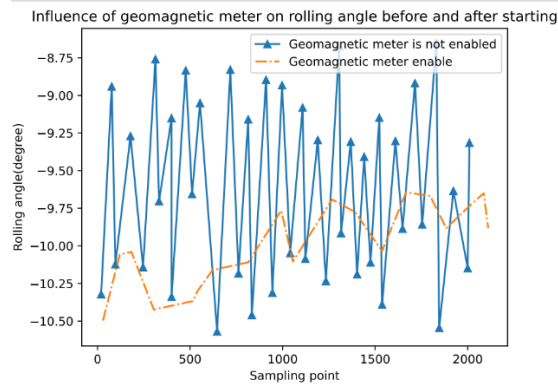
Figure 11: Effect of geomagnetic meter on cross-roll angle before and after enabling.

Mode	Pitch angle(degree)	Roll angle(degree)Heading	Angle of heading(degree)
MARG-RMSE	0.3228	0.3342	0.3085
IMU-RMSE	0.9852	1.1833	N/A

Table 3: Comparison of RMSE in IMU and MARG modes.

4.2.4 Whole-Body Motion Capture Test

Multi-node human motion capture is more challenging than single-node posture tracking. Because tracking of human body location has yet to be developed, the following tests only include tracking human body motion in this study. Therefore, all the tests entail only the following: The physical impact of the whole-body motion capture is depicted in Figure 12.
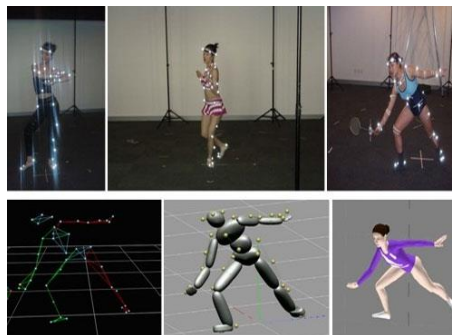
Figure 12: Demonstration of the whole body motion capture system.

The subject only needs to take a stand-alone action and then click the calibration button in the software interface to begin the system's calibration process. Except for the nodes on the back, which are not strictly necessary, they must be worn in the center for calibration. A full-body motion capture example is shown in Figure 12. Figure 12 has a screenshot of the appropriate model action at the bottom and five actions performed by the natural person at the top. Additionally, Figure 12 demonstrates how this technology successfully captures the most fundamental human body

movements. The model human's movement in the figure is stiff because the system only has ten nodes, and there is still a gap with the natural human model. This technology will not wholly track the body's movement, showing curvature if the user makes an action like lowering the waist. Additionally, to increase the authenticity of the model presentation, the model's bones can be modified in the actual application by the length of the human skeleton.

5   CONCLUSIONS

Applications for motion capture systems in healthcare, gaming, entertainment, and physical education look promising. Due to its site-independent, easy-to-use, and practical benefits, multi-sensor-based motion capture has drawn much attention. The secondary development of some commercialized items is severely constrained by their high cost and the vital confidentiality of the underlying technology. This research investigates a multi-sensor-based online physical education motion capture system that fully implements a multi-node motion capture system. The algorithms and methods covered in this study lower the cost of employing such systems, support the popularity of multi-sensor-based motion capture systems, and give researchers access to a system with a high degree of secondary development. Ethical considerations surrounding data privacy and the responsible use of AI-generated insights are paramount. Protecting students' privacy and ensuring the ethical handling of sensitive health-related data are essential for the system's ethical implementation.

Zhilong Zhao, https://orcid.org/0009-0001-9088-8132
Xinyang Xing, https://orcid.org/0000-0002-8869-2181

REFERENCES

[1]   Abd, A.; Fahd, Mohammed A.; Zambare, S. P.:   New Species of Flesh Fly (Diptera: Sarcophagidae) Sarcophaga (Liosarcophaga) Geetai in India, J Entomol Zool Stud 4(3), 2016, 314-318.
[2]   Al-Azab, A.M.; Zaituon, A.A.; Al-Ghamdi, K.M.; Al-Galil, F.M.A.: Surveillance of Dengue Fever Vector Aedes Aegypti in Different Areas in Jeddah City Saudi Arabia, Adv. Anim. Vet. Sci, 10(2), 2022, 348-353. https://doi.org/10.17582/journal.aavs/2022/10.2.348.353
[3]   Ali, R.; Muhammad, Hameed S.; Sungyoung, L.: Rough Set-Based Approaches for Discretization: A Compact Review, Artificial Intelligence Review 44(2), 2015, 235-263. https://doi.org/10.1007/s10462-014-9426-2
[4]   Al-Mekhlafi, Fahd A.; Reem, Alajmi A.; Zainab, A.; Fahd, Mohammed Abd Al G.; Pawandeep, K.; Muhammad, Al-W.; Mohammed, Al-Khalifa S.: A Study of Insect Succession of Forensic Importance: Dipteran Flies (Diptera) in Two Different Habitats of Small Rodents in Riyadh City, Saudi Arabia, Journal of King Saud University-Science 32(7), 2020, 3111-3118. https://doi.org/10.1016/j.jksus.2020.08.022
[5]   Alqahtani, Abdulaziz R.; Ahed, B.; Sayed, Amer A.M.; Fahd, Mohammed Abd Al G.; Mervat, Ahmed A.; Zuhair, Amr S.: Intraspecific Molecular Variation Among Androctonus Crassicauda Populations Collected from Different Regions in Saudi Arabia, Journal of King Saud University-Science 34(4), 2022, 101998. https://doi.org/10.1016/j.jksus.2022.101998
[6]   Alsubari, S. N.; Deshmukh, S. N.; Alqarni, A. A.; Alsharif, N. H. T.: Data Analytics for the Identification of Fake Reviews Using Supervised Learning, CMC-Computers, Materials & Continua, 70(2), 2022, 3189–3204. https://doi.org/10.32604/cmc.2022.019625
[7]   Bansode, S. A.; More, V. R.: Zambare, S. P.; Fahd. M.: Effect of Constant Temperature (20 0C, 25 0C, 30 0C, 35 0C, 40 0C) on the Development of the Calliphorid Fly of Forensic Importance, Chrysomya megacephala Journal of Entomology and Zoology Studies, 4(3), 2016,

193-197.

[8]   Cai, G.; Fang, Y.; Wen, J.; Mumtaz, S.; Song, Y. Frascolla, V.: Multi-Carrier M-ary DCSK System with Code Index Modulation: An Efficient Solution for Chaotic Communications, in IEEE Journal of Selected Topics in Signal Processing, 13(6), 2019, 1375-1386. https://doi.org/10.1109/JSTSP.2019.2913944

[9]   Chandra, K.; Marcano, A. S.; Mumtaz, S.; Prasad, R. V.; Christiansen, H. L.: Unveiling Capacity Gains in Ultradense Networks: Using mm-Wave NOMA, in IEEE Vehicular Technology Magazine, 13(2), 2018, 75-83. https://doi.org/10.1109/MVT.2018.2814822

[10] Chang, K. E.; Zhang, J.; Huang, Y. S.; Liu, T. C.; Sung, Y. T.: Applying Augmented Reality in Physical Education on Motor Skills Learning, Interactive Learning Environments, 28(6), 2020, 685-697. https://doi.org/10.1080/10494820.2019.1636073

[11] Di, W.; Yin, L.; Maoen, H.; Chunjiong, Z.; Li, J.; Deep Reinforcement Learning-Based Path Control and Optimization for Unmanned Ships, Wireless Communications and Mobile Computing, 2022(7135043), 2022, 8. https://doi.org/10.1155/2022/7135043

[12] Goldsmith, J. A.; Trepeck, C.; Halle, J. L.; Mendez, K. M.; Klemp, A.; Cooke, D. M.; Zourdos, M. C.: Validity of the Open Barbell and Tendo Weightlifting Analyzer Systems Versus the Optotrak Certus 3D Motion-Capture System for Barbell Velocity, International Journal of Sports Physiology and Performance, 14(4), 2019, 540-543. https://doi.org/10.1123/ijspp.2018-0684

[13] Grigg, J.; Haakonssen, E.; Rathbone, E.; Orr, R.; Keogh, J. W.: The Validity and Intra-Tester Reliability of Markerless Motion Capture to Analyse Kinematics of the BMX Supercross Gate Start, Sports Biomechanics, 17(3), 2018, 383-401. https://doi.org/10.1080/14763141.2017.1353129

[14] Lerma, N.; Gulgin, H.: Agreement of a Portable Motion Capture System to Analyze Movement Skills in Children, Measurement in Physical Education and Exercise Science, 2022, 1-9. https://doi.org/10.1249/01.mss.0000882100.25528.ad

[15] Li, H.; Cui, C.; Jiang, S.: Strategy for Improving the Football Teaching Quality by AI and Metaverse-Empowered in Mobile Internet Environment, Wireless Networks, 2022, 1-10. https://doi.org/10.1007/s11276-022-03000-1

[16] Liu, Q.; Liu, C.; Wang, Y.: etc. Integrating External Dictionary Knowledge in Conference Scenarios The Field of Personalized Machine Translation Method, Journal of Chinese Informatics, 33(10), 2019, 31-37.

[17] Palanisamy, S.; Thangaraju, B.; Khalaf, O.I.; Alotaibi, Y.; Alghamdi, S.; Alassery, F.: A Novel Approach of Design and Analysis of a Hexagonal Fractal Antenna Array (HFAA) for Next-Generation Wireless Communication, Energies 14, 2021, 6204. https://doi.org/10.3390/en14196204

[18] Pilati, F.; Faccio, M.; Gamberi, M.; Regattieri, A.: Learning Manual Assembly Through Real-Time Motion Capture for Operator Training with Augmented Reality, Procedia Manufacturing, 45, 2020, 189-195. https://doi.org/10.1016/j.promfg.2020.04.093

[19] Protopapadakis, E.; Voulodimos, A.; Doulamis, A.; Camarinopoulos, S.; Doulamis, N.; Miaoulis, G.: Dance Pose Identification from Motion Capture Data: A Comparison of Classifiers, Technologies, 6(1), 2018, 31. https://doi.org/10.3390/technologies6010031

[20] Qiu, S.; Zhao, H.; Jiang, N.; Wu, D.; Song, G.; Zhao, H.; Wang, Z.: Sensor Network Oriented Human Motion Capture Via Wearable Intelligent System, International Journal of Intelligent Systems, 37(2), 2022, 1646-1673. https://doi.org/10.1002/int.22689

[21] Saghezchi, Firooz B.; Ayman, R.; Jonathan, R.; Tasos, D.: Coalition Formation Game Toward Green Mobile Terminals in Heterogeneous Wireless Networks, IEEE Wireless Communications 20(5), 2013, 85-91. https://doi.org/10.1109/MWC.2013.6664478

[22] Sgro, F.; Quinto, A.; Platania, F.; Lipoma, M.: Assessing the Impact of a Physical Education Project Based on Games Approach on the Actual Motor Competence of Primary School Children, Journal of Physical Education and Sport, 19, 2019, 781-786.

[23] Steinberg, C.; Zühlke, M.; Bindel, T.; Jenett, F.: Aesthetic Education Revised: A Contribution

to Mobile Learning in Physical Education, German Journal of Exercise and Sport Research, 50(1), 2020, 92-101. https://doi.org/10.1007/s12662-019-00627-9

[24] Wang, T. J.: A Study on Utilizing 3D Motion-Capture Analysis to Assist in Chinese Opera Teaching, Research in Dance Education, 23(2), 2022, 194-222. https://doi.org/10.1080/14647893.2020.1812559

[25] Yang, Y.: The Innovation of College Physical Training Based on Computer Virtual Reality Technology, Journal of Discrete Mathematical Sciences and Cryptography, 21(6), 2018, 1275-1280. https://doi.org/10.1080/09720529.2018.1526400